Journal of
Marine Science and Engineering

MDPI

Article

Crashworthiness and Impact Resilience of Offshore Wind Turbines Protected by Honeycomb Sandwich Fenders

Kunpeng Liu [1], Haoda Huang [1,2,*], Wanyong Zhang [1], Wanfu Zhang [1] and Chun Li [1]

[1] School of Energy and Power Engineering, University of Shanghai for Science and Technology, Shanghai 200093, China; 251210034@st.usst.edu.cn (K.L.); zwy010227@163.com (W.Z.); wfzhang@usst.edu.cn (W.Z.); chunli.usst@gmail.com (C.L.)
[2] School of Engineering and Architecture, University College Cork, College Rd., T12 K8AF Cork, Ireland
* Correspondence: hhd_usst@163.com

Abstract

Owing to transportation, installation, grid-connection, and maintenance requirements, nearshore offshore wind farms are often located close to busy shipping routes, substantially increasing the risk of ship–offshore wind turbine (OWT) collisions. To enhance the impact resilience of OWT support structures against ship collisions, a novel honeycomb sandwich fender is proposed for tower protection. Nonlinear transient analyses were performed using ANSYS/LS-DYNA to simulate a 5000 t ship traveling at 2 m/s and colliding with a 4 MW OWT supported by a single-column tripod foundation. The effects of rubber and aluminum foam cores on the crashworthiness and protective performance of the fender were compared. The results show that the rubber core stores collision energy through recoverable large deformation and releases most of the stored energy during unloading, resulting in pronounced energy restitution and prolonged structural excitation. By contrast, the aluminum foam core dissipates 7.5 MJ through cell-wall buckling, progressive crushing, and plastic collapse, corresponding to 75% of the initial kinetic energy of the ship. Compared with the rubber-core fender, the higher initial stiffness of the aluminum foam increases the peak contact force by 23.1%, from 13.0 to 16.0 MN. However, its irreversible energy-dissipation mechanism reduces the maximum tower-top displacement by 40.0%, from 1.25 to 0.75 m, and decreases the residual tower stress after three successive collisions by 25.0%, from 200 to 150 MPa. These results demonstrate that, despite transmitting a higher peak contact force, the aluminum foam fender provides more effective overall protection under the collision conditions considered because of its greater irreversible energy-dissipation capacity.

Keywords: offshore wind turbine; honeycomb sandwich structure; nonlinear transient response; crashworthiness; impact resilience

Academic Editor: Chia-Cheng Tsai

Received: 23 July 2026
Revised: 13 August 2026
Accepted: 13 August 2026
Published: 15 August 2026

1. Introduction

Offshore wind power is an important pathway for promoting the clean and low-carbon transition of the energy system and provides essential support for achieving carbon-peaking and carbon-neutrality goals [1]. Compared with onshore wind resources, offshore wind resources generally feature higher wind speeds, more stable wind directions, lower turbulence intensity, and greater suitability for large-scale development, making offshore wind power an important direction for wind energy development in coastal regions [2]. To reduce the construction and subsequent operation and maintenance costs of offshore wind power projects, many existing offshore wind farms are located in coastal waters with dense maritime traffic, substantially increasing the risk of ship–offshore wind turbine (OWT) collisions [3,4]. Therefore, investigating ship–OWT collisions is of considerable significance for improving the safety of OWT systems and reducing accident risks.

Numerous studies have been conducted on OWTs subjected to ship impacts. Moulas et al. [5] proposed a nonlinear finite element method for calculating the structural damage caused by ship collisions. Their analyses of collision-induced damage to monopile and jacket foundations showed that ship velocity and impact location were the most critical factors affecting damage severity. Bela et al. [6] developed finite element models to investigate the effects of impact velocity, impact location, wind direction, soil stiffness, and deformation capacity on the collision process. Rigid and deformable ship models were employed to impact an OWT monopile foundation. The results indicated that a slight variation in ship velocity could cause a substantial difference in kinetic energy, resulting in structural responses ranging from minor damage to complete collapse. In the most severe case, the OWT foundation collapsed directly toward the ship. Ren et al. [7] simulated the dynamic response and structural damage of a 5 MW spar-type floating OWT subjected to ship collision. Through comparisons with FAST and an eight-degree-of-freedom simplified model developed in MATLAB, the contact force, displacement, acceleration, structural damage, and energy dissipation during collisions at different velocities were analyzed. The results showed that the maximum collision force and maximum tower-top displacement were approximately linearly related to the initial velocity. The maximum tower-top acceleration exceeded 0.2 g during the collision, seriously affecting the normal operation of the OWT.

However, the above studies mainly focused on the dynamic responses and consequences of OWTs impacted by different types of ships under various collision conditions, without investigating measures to reduce collision-induced damage and protect OWT foundations. Anti-collision measures have been widely applied to bridge piers, offshore oil and gas platforms, and other marine structures. Wang et al. [8] employed the finite element method to investigate the energy evolution and structural responses of protected bridge piers subjected to impacts from ships of different deadweights. The results showed that most of the system's internal energy was dissipated by the fender, whereas the pier and ship bow absorbed relatively little energy, indicating that the fender could effectively protect both the pier and the ship. Yan et al. [9] proposed a modular protective device for protecting bridge piers against debris-flow impacts and investigated the effects of material and geometric parameters on its performance using a validated finite element model. With the development of the offshore wind industry, fenders have gradually been applied to OWTs. Liu et al. [10] designed a fender for an OWT monopile foundation and optimized its material and structural thickness. The results demonstrated that the optimized fender provided improved protective performance and enhanced the safety of the OWT foundation. The proposed method was also applicable to jacket and tripod foundations. Han et al. [11] proposed four fender configurations comprising different combinations of rubber and aluminum foam. ANSYS/LS-DYNA (ANSYS LS-DYNA R13.0.0 within ANSYS 2022 R1) was employed to calculate the maximum contact force, energy evolution, plastic strain, and other response parameters. The results showed that the aluminum foam fender exhibited better anti-collision performance. In recent years, honeycomb structures have attracted considerable attention because of their high strength, low weight, and high specific energy absorption [12]. Zhang et al. [13] experimentally and numerically investigated the indentation response and energy absorption of aluminum honeycomb sandwich panels subjected to low-velocity impacts. The results showed that the sandwich

https://doi.org/10.3390/jmse14161509

panels exhibited substantial energy-absorption capacity under impact loading and that the adhesive layer had an important influence on energy distribution and absorption. Rathod et al. [14] compared the ballistic limits, failure modes, and energy-absorption characteristics of aramid and aluminum honeycomb sandwich structures through high-velocity impact tests and numerical simulations. The results indicated that the aluminum honeycomb sandwich structure exhibited greater penetration resistance, whereas the aramid honeycomb sandwich structure performed better in terms of energy absorption and specific energy absorption. Chang et al. [15] investigated the energy-absorption characteristics of different composite honeycomb sandwich structures through drop-weight impact tests and numerical simulations. Their results showed that the material combination and cell size significantly affected the impact force, structural deformation, and energy absorption. However, existing studies have mainly focused on aerospace structures and high-velocity projectile impacts, while applications of honeycomb structures to the collision protection of OWT towers remain limited.

To address this gap, a honeycomb sandwich fender is proposed for the collision protection of a 4 MW OWT supported by a single-column tripod foundation, and nonlinear transient analyses are conducted in LS-DYNA to simulate a head-on collision with a 5000 t ship traveling at 2 m/s. This study investigates the influence of core material on the crashworthiness and protective performance of the fender by comparing rubber and aluminum foam cores. Energy absorption and contact-force responses are examined to characterize the energy-dissipation and load-transfer behavior of the fender, whereas tower-top displacement and tower stress–strain responses under repeated collisions are evaluated to assess its immediate and cumulative protective effects. The findings provide a basis for core-material selection and the crashworthy design of honeycomb sandwich fenders for OWTs.

2. Methodology

2.1. Motion Equation

The collision between a ship and an offshore wind turbine is a highly nonlinear dynamic process involving large deformation, material nonlinearity, and contact. Following spatial discretization, the semi-discrete equation of motion at time step (n) in the LS-DYNA explicit formulation can be expressed as [16]:

$$\mathbf{M}\mathbf{a}_n = \mathbf{P}_n - \mathbf{F}_n + \mathbf{H}_n \tag{1}$$

where $\mathbf{M}$ is the diagonal lumped mass matrix; $\mathbf{a}_n$ is the nodal acceleration vector; $\mathbf{P}_n$ is the external and body-force load vector, including the nodal contributions generated by contact interaction; $\mathbf{F}_n$ is the stress-divergence vector representing the internal forces generated by the element stresses; and $\mathbf{H}_n$ is the hourglass resistance vector. The hourglass resistance is generated numerically to suppress the zero-energy deformation modes of under-integrated elements and is not an independently applied physical force.

2.2. Contact Algorithm

To accurately model the contact and frictional interaction between the ship and the OWT tower while preventing nonphysical penetration, the automatic surface-to-surface contact algorithm (*CONTACT_AUTOMATIC_SURFACE_TO_SURFACE) was employed in LS-DYNA.The friction force between different structures during the collision can be expressed as follows [17]:

$$F_y = \mu \mid f_s \mid \tag{2}$$

$$\mu = \mu_d + (\mu_s - \mu_d)e^{-\alpha v} \tag{3}$$

where F_y is the friction force; f_s is the nodal contact force; μ is the friction coefficient; μ_d and μ_s are the dynamic and static friction coefficients, respectively; α is the decay coefficient; and v is the relative contact velocity. According to Dai et al. [18], a head-on collision causes more severe damage to an offshore wind turbine than lateral and drifting collisions. Because the present study focuses on the effects of different materials on the impact resistance of the fender, only a head-on collision directly against the honeycomb structure was simulated.

2.3. Turbulent Wind

Offshore wind turbines operate in complex marine environments characterized by high wind speeds and turbulence intensity. Because wind turbine blades and towers are slender and flexible structures, wind loading has a significant influence on their global dynamic responses. Current methods for calculating wind loads on wind turbines mainly include computational fluid dynamics simulations, the free-vortex wake method, and blade element momentum theory (BEMT). Among these approaches, BEMT is a classical method for evaluating wind turbine loads and has been widely applied in aerodynamic calculations because of its simplicity and computational efficiency. It primarily combines blade element theory with momentum theory [19]. In accordance with the IEC standard, the Kaimal turbulence power spectral density was adopted, and the turbulent wind field was generated using TurbSim. The resulting wind field was imported into FAST to calculate the rotor thrust at a wind speed of 11.4 m/s. The calculated rotor thrust was subsequently applied through the load-control option in ANSYS/Workbench. Figure 1 presents the three-dimensional turbulent wind field.

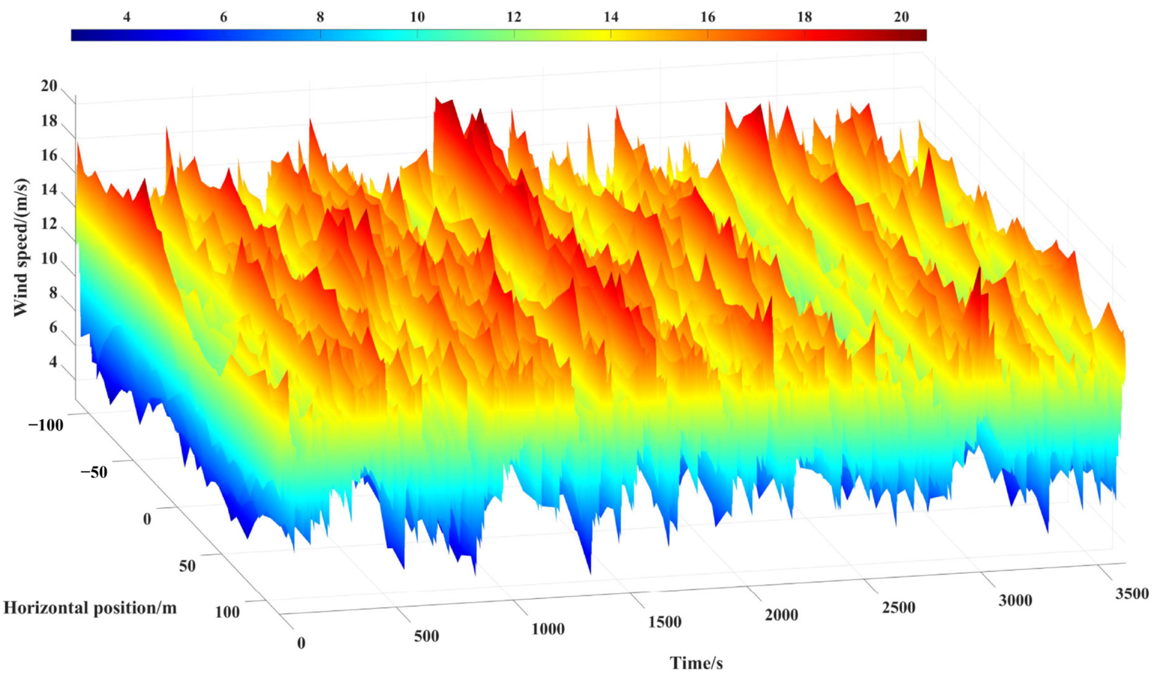

Figure 1. Three-dimensional model of turbulent wind.

3. Constitutive Materials

3.1. Steel

Q235 steel was assigned to the ship, tripod foundation, and offshore wind turbine tower, whereas Q345 steel was used for the inner and outer face sheets of the honeycomb sandwich fender [20,21]. The mechanical properties and Cowper–Symonds parameters of the Q235 and Q345 structural steels are summarized in Table 1, where ρ is the material density, E is Young's modulus, ν is Poisson's ratio, σ_0 is the initial yield stress, E_t is the tangent modulus, β is the hardening parameter, C and P are the Cowper–Symonds parameters describing the strain-rate effect, and ε is the failure strain.

Table 1. Material parameters of Q235 and Q345.

Parameters/Unit	The Type of Materials	
	Q235	Q345
$\rho/(\mathrm{kg \cdot m^{-3}})$	7850	7850
E/GPa	210	212
υ	0.27	0.31
σ_0/MPa	235	345
$E_\mathrm{t}/\mathrm{MPa}$	1180	1291
β	0	0
C/s^{-1}	40.4	40.4
P	5	5
ε	0.34	0.34

During a ship–OWT collision, the structural materials undergo rapid deformation, resulting in pronounced strain-rate variations that affect the dynamic response of the OWT [22]. Therefore, a nonlinear plastic material model incorporating strain-rate sensitivity was adopted in LS-DYNA to represent the material behavior under impact loading [23]. The model is based on the Cowper–Symonds constitutive equation and accounts for the effects of strain rate on the mechanical response of the material:

$$\sigma_y = \left[1 + \left(\frac{\dot{\varepsilon}}{C}\right)^{1/P}\right](\sigma_0 + \beta E_P \varepsilon^P_{eff}) \quad (4)$$

where σ_y is the dynamic yield stress; σ_0 is the initial yield stress; $\dot{\varepsilon}$ is the plastic strain rate; ε^P_{eff} is the effective plastic strain; E_P is the plastic hardening modulus; β is the hardening parameter; E is Young's modulus; and C and P are the Cowper–Symonds parameters describing the strain-rate effect.

3.2. Ogden

Rubber materials exhibit high elasticity, large deformation capacity, and favorable impact-cushioning performance and are therefore widely used in anti-collision and vibration-mitigation devices. During a ship collision, the rubber layer undergoes substantial deformation, and its stress–strain relationship exhibits pronounced material nonlinearity, which cannot be accurately represented using conventional linear elastic models. Therefore, the rubber was modeled as an isotropic and nearly incompressible hyperelastic material, and the Ogden model available in LS-DYNA was adopted to describe its large-deformation behavior. This model uses the three principal stretch ratios, λ_1, λ_2, and λ_3, as the fundamental variables and can effectively characterize the nonlinear mechanical behavior of rubber under different deformation states [24]. The strain-energy density function is expressed as follows:

$$W = \sum_{n=1}^{N} (\mu_n/\alpha_n)[J^{-\alpha_n/3}(\lambda_1^{\alpha_n} + \lambda_2^{\alpha_n} + \lambda_3^{\alpha_n})] - 3 + 4.5K(J^{1/3} - 1)^2 \quad (5)$$

where W is the strain-energy density; μ_n and α_n are material constants; λ_i is the principal stretch ratio ($i = 1, 2, 3$); K is the initial bulk modulus; and J is the volume ratio. By assuming $J = 1$, Equation (5) can be simplified as follows:

$$W = \sum_{n=1}^{N} \frac{\mu_n}{\alpha_n} [(\lambda_1^{\alpha_n} + \lambda_2^{\alpha_n} + \lambda_3^{\alpha_n}) - 3] \tag{6}$$

The nominal tensile stress of the Ogden rubber under uniaxial loading is expressed as follows, and the corresponding material parameters are listed in Table 2:

$$\sigma = \sum_{n=1}^{N} \mu_n (\lambda^{\alpha_n - 1} - \lambda^{-1-\alpha_n/2}) \tag{7}$$

Table 2. The parameters of the Ogden model.

μ_1/MPa	α_1	μ_2/MPa	α_2
3.00071	0.719155	0.1026	−4.771

3.3. Aluminum Foam

Aluminum foam is a porous metallic material consisting of an aluminum or aluminum-alloy matrix containing numerous pores. It is characterized by low density, high specific strength, and high specific energy-absorption capacity and has therefore been widely used in aerospace, transportation, and collision-protection applications [25]. Under compressive loading, aluminum foam generally undergoes three deformation stages: elastic deformation, cell-wall buckling and collapse, and densification, accompanied by significant volumetric plastic deformation. Unlike dense metals, its yielding behavior depends not only on deviatoric stress but also strongly on hydrostatic pressure. Therefore, the conventional von Mises yield criterion cannot accurately describe its crushing response. Accordingly, the *MAT_DESHPANDE_FLECK_FOAM material model in LS-DYNA was adopted to represent the mechanical behavior of aluminum foam. This model was proposed by Deshpande and Fleck [26] based on an isotropic continuum framework. The evolution of the flow stress is expressed as follows:

$$\Phi = \sigma_p + \gamma \frac{\hat{\varepsilon}}{\varepsilon_D} + \alpha_2 \ln \left[1/(1 - \left(\frac{\hat{\varepsilon}}{\varepsilon_D} \right)^{\beta}) \right] \tag{8}$$

where σ_p is the initial flow stress; γ is the linear hardening modulus; $\hat{\varepsilon}$ is the equivalent plastic strain; ε_D is the densification strain; α_2 is the nonlinear hardening modulus; and β is the nonlinear hardening exponent.

The constitutive parameters of the Deshpande–Fleck model are listed in Table 3, where E is Young's modulus, ρ is the density, ν is Poisson's ratio, and α is the yield-surface shape parameter.

Table 3. Parameters used in the Deshpande and Fleck model.

Parameters/Unit	Value
σ_P/MPa	0.6
ν	0.3
E/MPa	370
ρ/kg · m^{-3}	178
γ/MPa	3.23
ε_D	1.8
α	2.119
α_2/MPa	6.2
β	4.23
Volumetric strain	0.01

4. Model Establishment

4.1. Tripod

A 4 MW offshore wind turbine supported by a single-column tripod foundation was considered in this study. The system consists of upper and lower assemblies. The upper assembly comprises the wind turbine components, including the hub, blades, generator system, and nacelle, whereas the lower assembly serves as the supporting foundation and consists of the central column, horizontal braces, diagonal braces, and Steel pipe column. The principal structural parameters are listed in Table 4, and the finite element model and mesh sizes are illustrated in Figure 2. Because the upper assembly has a complex geometry and is located far from the collision region, it was simplified using the lumped-mass method [27], with its equivalent mass concentrated at the tower top.

Table 4. Main structural parameters of the tripod foundation [28].

Structural Component	Outer Diameter/m	Wall Thickness/mm
Central column	4.0–5.8	50–80
Steel pipe column	2.7	35–40
Horizontal brace	1.4–1.9	28–35
Diagonal brace	2.2–3.0	35–55

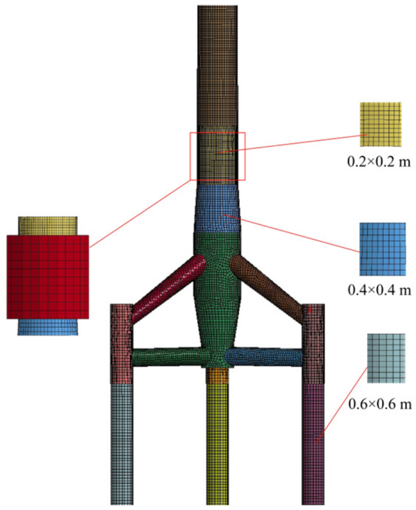

Figure 2. Finite element of tripod.

During the collision, the soil surrounding the pile foundation primarily restrains its lateral movement. According to DNV-OS-J101, the horizontal displacement of steel pipe piles at the mudline is generally limited to less than 20 mm for large offshore wind turbines designed under the Accidental Limit State [29]. Furthermore, offshore wind turbine pile foundations and their connections are commonly reinforced by grouting or similar measures. Therefore, following previous numerical studies of ship–offshore wind turbine collisions, the soil domain was not modeled explicitly. Instead, the pile segments embedded below the mudline were treated as a rigidly constrained region, and all degrees of freedom in this region were fixed.

4.2. Ship

A representative ship with a raked bow was selected for the collision analysis. The ship was positioned to collide head-on with the offshore wind turbine tower, with the bow defined as the primary impact region. Its principal dimensions are summarized in Table 5. To improve numerical accuracy in the impact region, the bow was locally refined using elements measuring 0.10 m × 0.10 m, whereas a coarser mesh of 0.25 m × 0.25 m was applied to the remaining regions, as shown in Figure 3.

Table 5. Principal dimensions of the ship.

Parameter of Ship/Unit	Overall Length/m	Molded Breadth/m	Molded Depth/m	Ship Mass (Including Longitudinal Added Mass)/t
Value	108	17	8	5000

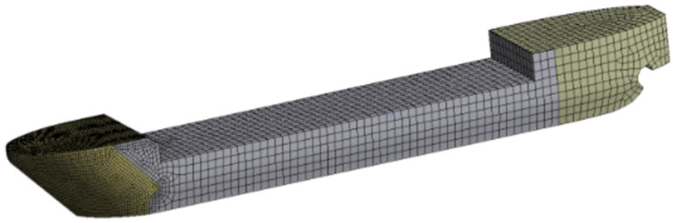

Figure 3. Finite element model of the ship.

During a ship–OWT collision, the hydrodynamic interaction between the ship and the surrounding seawater cannot be neglected. However, a fluid–structure interaction model requires a large computational domain and considerable computational resources [30]. Therefore, the added-mass method was adopted to represent the hydrodynamic inertia of the surrounding seawater. Because the ship collided head-on with the OWT, the added-mass coefficient of 0.05 [31] was applied in the longitudinal direction of the ship, corresponding to the direction of travel and impact. The ship mass of 5000 t used in the numerical model is the effective collision mass and already includes the longitudinal added mass. Added masses in the transverse and vertical directions and hydrodynamic rotational inertia were not considered in the present analysis.

4.3. Fender

The present study focuses on the influence of honeycomb core material on the protective performance of the fender. To isolate the material effect, the geometric parameters of the rubber-core and aluminum foam-core fenders were kept identical. The cell-edge length of the regular hexagonal honeycomb was set to 0.6 m. A smaller cell size would substantially increase the number of cell walls and finite elements, thereby increasing the computational cost and complicating the identification of progressive compression and failure modes. The selected cell size therefore facilitates the interpretation of cell-level deformation during collision while maintaining a manageable computational cost. The inner and outer diameters of the fender were 5.0 and 8.0 m, respectively, and its height was 7.5 m. The inner and outer face sheets were both 0.1 m thick, and the radial thickness of the honeycomb core was 1.3 m. The honeycomb core and face sheets were modeled using solid elements, and their interfaces were connected using a tied constraint (*CONTACT_TIED_SURFACE_TO_SURFACE). Considering the regular geometry of the fender and the large compressive deformation expected during collision, the entire structure was discretized using structured hexahedral solid elements. A similar element strategy has been adopted in explicit impact analyses of sandwich structures containing rubber and aluminum foam cores [32]. The element size was 0.25 × 0.25 m, and the resulting finite element model is shown in Figure 4. Although the two fenders had identical geometries and core volumes, they were not mass-equivalent because rubber and aluminum foam have different densities. Therefore, the present comparison represents the direct replacement of the core material within the same fender geometry rather than a comparison under an equal-mass condition.

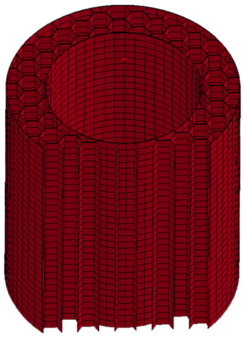

Figure 4. Finite element model of the fender.

The honeycomb unit cell and its deformation modes are illustrated in Figure 5. Under transverse compression, the force and bending moment can be expressed as follows:

$$F_x = \sigma_x(a + b\sin\theta)h \tag{9}$$

$$M_x = 1/2F_x b\sin\theta \tag{10}$$

where h is the cell height. Because all edges of the regular hexagonal honeycomb cell are equal in length, the included angle is 30°.

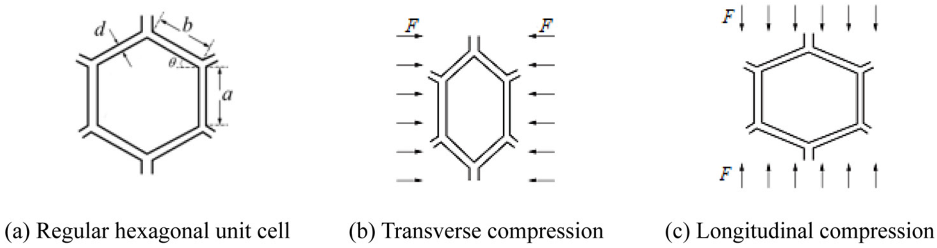

Figure 5. Honeycomb cell and deformation.

Similarly, under longitudinal compression, the force and bending moment can be expressed as follows:

$$F_y = \sigma_y\cos\theta \tag{11}$$

$$M_y = 1/2F_y b\cos\theta \tag{12}$$

4.4. Mesh Convergence Analysis

During the collision, the fender serves as the primary energy-absorbing component, and its mesh size may affect impact-load transmission, energy distribution, and the global response of the OWT. A mesh convergence analysis was therefore performed using an auxiliary solid-rubber fender while keeping all other model parameters unchanged. The continuous and regular geometry of this configuration reduces the influence of topology-dependent deformation and lowers the computational cost of evaluating multiple mesh schemes. Six characteristic element sizes of 0.05, 0.10, 0.15, 0.20, 0.25, and 0.30 m were considered for a collision case with an initial kinetic energy of 10 MJ. The system kinetic energy, internal energy, and hourglass energy, together with the peak contact force and maximum tower-top displacement, were selected as the convergence indicators.

As shown in Figure 6, the kinetic energy, internal energy, and hourglass energy histories obtained with the different mesh sizes exhibit highly consistent trends, indicating that the energy-transfer process is insensitive to mesh refinement within the investigated range. The peak contact force and maximum tower-top displacement also gradually converge as the mesh is refined. When the mesh size is reduced from 0.25 to 0.20 m, the relative differences in peak contact force and maximum tower-top displacement are 0.90% and 1.3%, respectively, demonstrating that the 0.25 m mesh can provide stable predictions of both impact-load transmission and the global structural response.

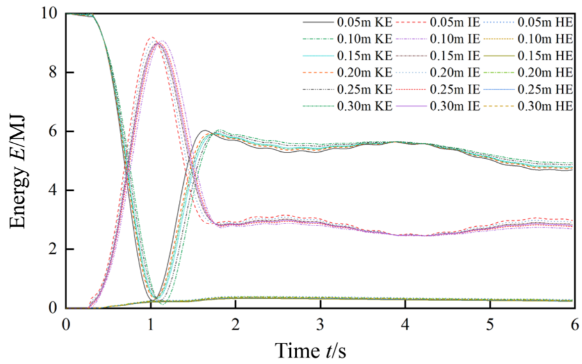

Figure 6. Energy time histories for different mesh sizes.

Although the 0.15 m mesh produces a relatively low hourglass energy, its computational time is approximately four times that of the 0.25 m mesh, whereas the differences in the principal response quantities are limited. Therefore, considering both numerical accuracy and computational efficiency, an element size of 0.25 m was adopted for the subsequent numerical simulations.

5. Results and Discussion

To elucidate the mechanisms through which different core materials influence the protective performance of the honeycomb fender, the numerical results obtained for the different material configurations were compared under identical collision conditions and structural parameters. The relationship between material characteristics and protective effectiveness was examined in terms of energy dissipation, contact force, and tower-top dynamic response. Because the conversion and dissipation of collision energy directly characterize the capacity of the fender to absorb and mitigate the kinetic energy of the ship, the energy response is analyzed first. The collision process begins with initial contact between the ship and the fender, followed by loading, unloading, and eventual separation. Owing to their different deformation and energy-dissipation mechanisms, the two core materials exhibit distinct peak-response times and contact durations. The characteristic times and durations of the two fender configurations are summarized in Table 6.

Table 6. Characteristic times and durations of the ship–fender interaction.

Event/Phase	Rubber Core (Ogden)	Aluminum Foam Core
Initial contact	0.3 s	0.3 s
Peak contact force	13.0 MN at 1.6 s	16.0 MN at 1.0 s
Ship–fender separation	2.5 s	1.4 s
Loading phase (contact → peak)	1.3 s	0.7 s
Unloading phase (peak → separation)	0.9 s	0.4 s
Total contact duration	2.2 s	1.1 s (−50%)

5.1. Energy Analysis

5.1.1. Overall Energy Balance of the Collision System

Figure 7 presents the energy time-history curves of the ship–OWT collision system equipped with the rubber and aluminum foam fenders. During the collision between the ship and the fender, energy conversion within the system follows the principle of energy conservation. Before impact, the system energy remains stable. Once the collision occurs, the kinetic energy of the ship decreases rapidly, while deformation of the fender under the impact load causes a substantial increase in internal energy. Consequently, the internal-energy curve increases rapidly and exhibits a trend opposite to that of the kinetic-energy curve. Surface-to-surface contact between the ship and the fender generates sliding-interface and damping energies, while element hourglass deformation produces hourglass energy. When the ship begins to separate from the fender, the kinetic energy rebounds and the internal energy decreases accordingly, indicating the release of part of the deformation energy stored in the fender. After the collision, the OWT undergoes small-amplitude reciprocating oscillations because of inertia. During this stage, kinetic and internal energies are converted into each other, resulting in periodic variations.

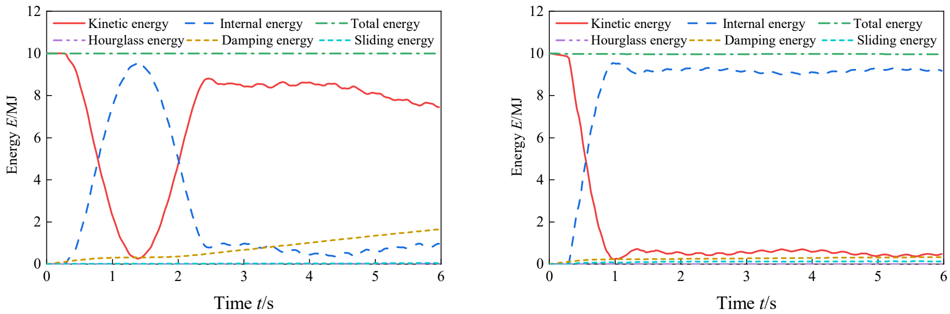

(**a**) Ogden (**b**) Aluminum foam

Figure 7. The energy curve.

The collision response generally evolved through elastic, elastoplastic, and plastic deformation stages. For the rubber-core honeycomb sandwich fender, the loading phase extended from initial contact at 0.3 s to the peak response at 1.6 s. During this phase, the large deformation of the rubber core rapidly converted the ship's kinetic energy into internal energy, causing the system's kinetic energy to decrease sharply to nearly zero while the internal energy increased nonlinearly to its peak value. During the subsequent unloading and separation phase from 1.6 to 2.5 s, the hyperelastic recovery of the rubber core released part of the stored strain energy back into the collision system. Consequently, the internal energy decreased to 0.9 MJ, while the kinetic energy rebounded to 9.0 MJ. This pronounced energy restitution demonstrates that the rubber core primarily stores collision energy through recoverable deformation rather than dissipating it irreversibly. The aluminum foam-core fender exhibited a distinctly different energy-conversion mechanism. Its loading phase extended from initial contact at 0.3 s to the peak response at 1.0 s. During the initial cell-wall buckling stage from 0.3 to 0.6 s, approximately 35% of the initial kinetic energy was absorbed. The core subsequently entered the plastic-collapse stage from 0.6 to 1.0 s, during which progressive folding of the cell walls and plastic deformation of the matrix converted most of the remaining kinetic energy into irreversible deformation energy. At 1.0 s, the system internal energy reached 9.2 MJ, while the kinetic energy decreased to 0.5 MJ. During the unloading and separation phase from 1.0 to 1.4 s, only a limited amount of energy was released because of the irreversible crushing of the aluminum foam. The total contact duration was therefore 1.1 s, which was 50% shorter than the 2.2 s obtained for the rubber-core configuration. With an energy-dissipation efficiency of approximately 94%, the aluminum foam-core fender exhibited a predominantly irreversible energy-dissipation pathway.

5.1.2. Evolution of Ship Energy

Figure 8 presents the evolution of ship energy during the collision. The rubber and aluminum foam honeycomb sandwich fenders produce distinctly different energy-response

https://doi.org/10.3390/jmse14161509

trends during the ship–OWT collision. For the rubber honeycomb sandwich fender, the ship energy decreases rapidly during the initial stage of collision, subsequently exhibits a pronounced recovery, and eventually stabilizes at a relatively high level. For the aluminum foam honeycomb sandwich fender, the ship energy also decreases rapidly at the beginning of the collision but remains close to zero thereafter, without a noticeable rebound. This difference is primarily attributed to the distinct mechanical response mechanisms of the two core materials during the collision.

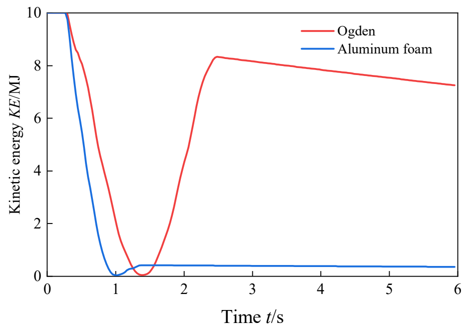

Figure 8. Ship kinetic energy.

At the onset of the collision, the ship possesses a high level of initial kinetic energy. When the ship comes into contact with the fender, the honeycomb core begins to deform and absorb energy. The rubber honeycomb structure exhibits a strong elastic recovery capability. Under impact loading, the rubber matrix undergoes large deformation and stores elastic strain energy. After the contact phase ends, elastic recovery converts part of the stored energy back into the kinetic energy of the ship, resulting in a pronounced secondary increase in the energy curve, which subsequently stabilizes at a relatively high level. This behavior indicates that not all of the initial kinetic energy is dissipated during the collision, resulting in a noticeable rebound of the ship.

In contrast, the aluminum foam honeycomb structure primarily absorbs energy through plastic deformation and pore collapse. Under impact loading, the cell walls of the aluminum foam undergo irreversible plastic folding and collapse, thereby dissipating a substantial amount of energy. Because plastic deformation develops extensively within the material and its elastic recovery is limited, the residual kinetic energy of the ship remains close to zero after the collision, without a pronounced energy rebound. The impact energy is converted into irreversible plastic deformation energy within a relatively short period, thereby limiting energy transmission to the OWT tower and mitigating collision-induced structural damage.

Therefore, the response of the rubber honeycomb structure is dominated by elastic deformation, resulting in substantial energy restitution during the later stage of the collision. In contrast, the aluminum foam honeycomb structure dissipates energy predominantly through irreversible plastic deformation, and the dissipated energy is not readily recovered.

5.1.3. Energy Absorption Characteristics of the Fender

After contact is established between the ship and the fender, the kinetic energy of the ship is redistributed into the deformation and internal energies of the collision-system components, primarily the fender, the kinetic energies of the fender and OWT, and energy dissipated through damping. Figure 9 presents the internal-energy time histories of the individual fender components. Part of the energy absorbed by the fender is stored as recoverable elastic strain energy and subsequently returned to the ship during unloading, corresponding to the post-peak decrease in the fender energy curve. The remaining energy is dissipated through irreversible structural deformation and damage, corresponding to the residual plateau of the energy curve after its decline.

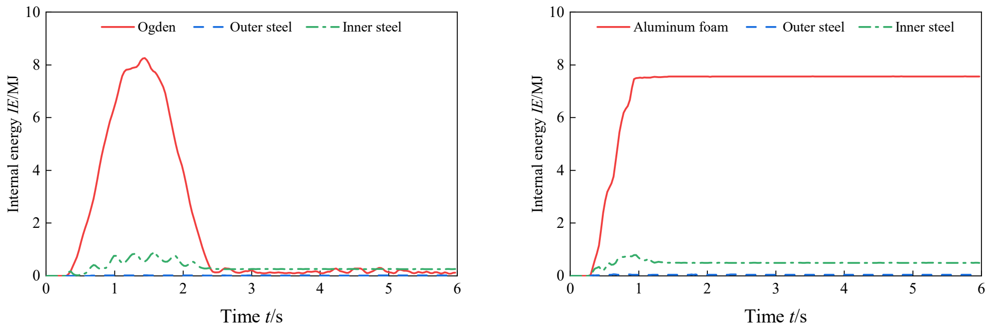

(**a**) Ogden (**b**) Aluminum foam

Figure 9. Internal energy time-history curve.

The internal energy of the aluminum foam core increased rapidly from the onset of the collision, reaching a peak of 7.5 MJ at 1.0 s, corresponding to 75% of the total collision energy, and subsequently remained stable. This response indicates that the aluminum foam converted a large proportion of the ship kinetic energy into irreversible plastic deformation energy through pore collapse and plastic deformation of the matrix, demonstrating a high energy-absorption capacity and limiting kinetic-energy transmission to the OWT tower. The final internal energies of the outer and inner steel face sheets were relatively low, at 0.7 and 0.3 MJ, respectively. These values represent the energy absorbed through plastic deformation of the steel face sheets. Their gradual energy evolution indicates that the face sheets primarily provided structural support and enhanced the overall stiffness of the fender, while the core served as the principal energy-absorbing component. Compared with the aluminum foam fender, the internal energy of the outer steel face sheet of the rubber fender approached 0.0 MJ after the collision. Following contact between the ship and the fender, the internal energy of the inner steel face sheet increased with oscillations, reached a peak of 0.85 MJ at 1.5 s, and then gradually decreased to 0.2 MJ at 2.5 s. Owing to its high elasticity, the rubber core stored the kinetic energy of the ship through large deformation during the collision. Its internal energy reached a peak of 8.2 MJ at 1.5 s, when the ship's kinetic energy decreased to approximately 0. As the rubber returned most of the stored deformation energy to the ship, the ship began to rebound and the internal energy of the rubber core decreased to 0.18 MJ. These results indicate that the aluminum foam honeycomb sandwich fender provides more effective collision protection by dissipating a greater proportion of the impact energy irreversibly and mitigating collision-induced damage to the OWT tower.

5.2. Contact Force

Figures 10 and 11 illustrate the collision processes of the honeycomb sandwich fenders with rubber and aluminum foam cores, respectively. The two core materials exhibit distinctly different deformation and failure modes under ship impact. The rubber core has relatively high tensile strength and elastic recovery capability. Consequently, its honeycomb structure can temporarily sustain high impact loads during the collision and rapidly recover after unloading. In contrast, the aluminum foam core primarily absorbs energy through plastic deformation and localized collapse of its cell walls. However, its relatively low tensile strength leads to material failure and fracture during the later stage of the collision, thereby altering its mechanical response.

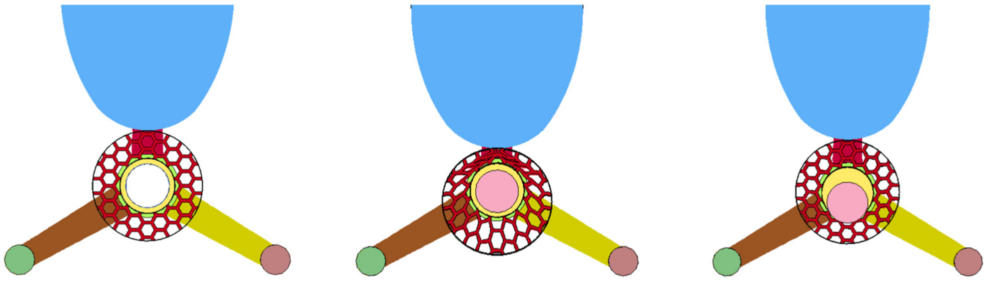

(a) 0.30 s (b) 1.35 s (c) 2.55 s

Figure 10. Collision process of the ogden protective device.

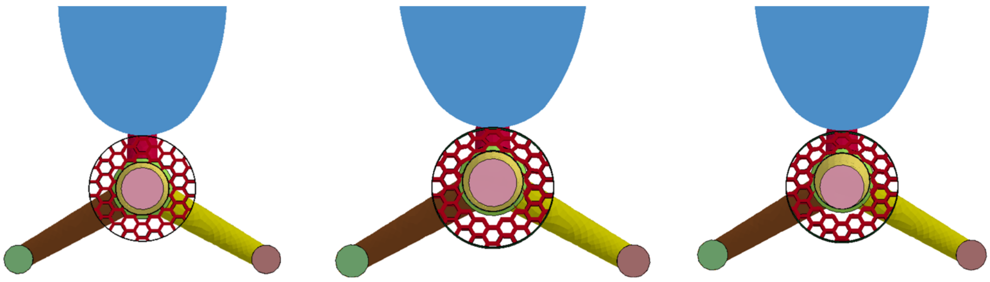

(a) 0.30 s (b) 1.05 s (c) 1.65 s

Figure 11. Collision process of the aluminum foam protective device.

Figure 12 presents the contact-force time histories during the collision. For the rubber-core honeycomb sandwich fender, the contact between the ship and the fender lasted approximately 2.5 s. The contact force increased gradually during the initial stage and exhibited multiple oscillatory peaks, reaching a maximum of 13.0 MN at 1.6 s. It subsequently decreased and approached zero when the contact ended at 2.5 s. These oscillations were primarily attributed to the progressive large deformation and local instability of individual honeycomb cells, together with the interactions between adjacent cell walls during compression. Consequently, the overall reaction force of the honeycomb structure increased progressively as the compressive deformation propagated through the core, rather than reaching its maximum immediately after initial contact. By contrast, the contact between the ship and the aluminum foam-core fender lasted only 1.4 s. The contact force increased rapidly during the initial stage, reached a maximum of 16.0 MN at 1.0 s, and then exhibited a pronounced oscillatory decay over a short period before decreasing to zero when the ship separated from the fender at 1.4 s. This response was primarily attributed to the higher initial stiffness and greater instantaneous load-carrying capacity of the aluminum foam, which maintained a relatively high deformation resistance during the initial stage and subjected the ship to a large reaction force within a short period. As the collision progressed, the internal cell walls of the aluminum foam underwent progressive buckling, crushing, and plastic collapse, thereby absorbing the kinetic energy of the ship and converting it into irreversible plastic deformation energy. Owing to the limited deformation-recovery capability of aluminum foam, no pronounced rebound or secondary contact-force peak occurred during the later stage of the collision. Therefore, after reaching its maximum value, the contact force of the aluminum foam-core fender exhibited an overall decreasing trend with superimposed oscillations.

Overall, the relatively high initial stiffness of the aluminum foam core provides the honeycomb sandwich fender with a high initial load-bearing capacity, while progressive cell-wall collapse causes the contact force to decay rapidly during the collision. This response reduces the duration of impact loading transmitted to the tower and tower-top nacelle. In contrast, although the rubber core possesses greater deformation capacity and elastic recovery capability and can resist material failure during the collision, it prolongs the contact process, thereby exposing the tower top to the coupled effects of vibration and impact over a longer period.

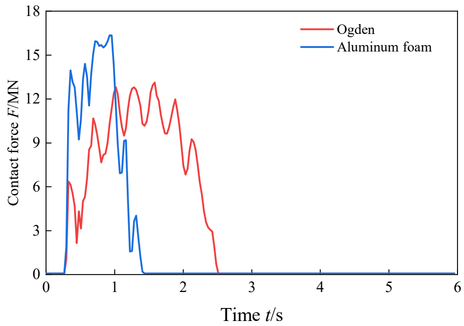

Figure 12. Contact force curve.

5.3. Top Displacement Response

During a ship–OWT collision, the dynamic response at the tower top is an important indicator for evaluating the collision effects and the protective performance of the fender. The tower-top response is primarily characterized by variations in displacement, velocity, and acceleration, which reflect the severity of the structural response induced by the collision and the energy-absorption effectiveness of the fender. Figure 13 presents the tower-top displacement time histories. Following the collision, the displacement responses associated with both the rubber and aluminum foam fenders initially develop in the negative direction, subsequently rebound in the positive direction, and then exhibit oscillatory behavior. However, pronounced differences are observed between the two fenders in terms of displacement amplitude and vibration period.

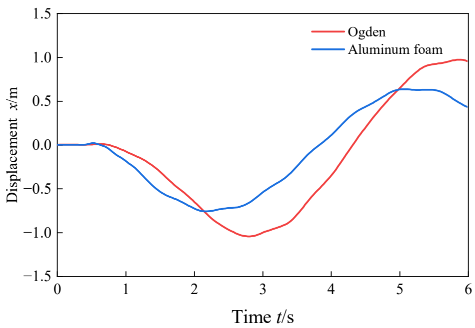

Figure 13. Tower-top displacement time-history curves.

For the rubber fender, the tower-top displacement exhibits a relatively large response in the negative direction during the early stage of structural motion, reaching a peak magnitude of 1.25 mat 3.0 s. This indicates that although the rubber core absorbs collision energy, its relatively low stiffness permits substantial tower-top displacement. Following the collision, the restoring force of the rubber causes the tower top to rebound rapidly. The displacement changes from negative to positive and reaches an opposite peak of 1.00 m at 6.0 s, after which relatively large displacement amplitudes persist. Thus, despite its energy-absorption and impact-cushioning capabilities, the low stiffness of the rubber core results in a large rebound displacement and prolonged structural vibration. In contrast, the maximum tower-top displacement associated with the aluminum foam fender is limited to 0.75 m, representing a reduction of approximately 40% relative to the rubber configuration. The higher initial stiffness and irreversible energy-absorption capacity of aluminum foam effectively suppress excessive tower-top displacement. Its porous structure dissipates collision energy through plastic deformation and cell-wall collapse, thereby reducing the subsequent rebound amplitude. During the following oscillatory stage, the aluminum foam fender produces smaller tower-top displacement peaks and a more moderate vibration amplitude. These results demonstrate that the aluminum foam fender is more effective than the rubber fender in dissipating collision energy and suppressing tower-top vibration. Its higher stiffness and irreversible crushing mechanism provide a clear advantage in limiting the maximum tower-top displacement.

5.4. Stress–Strain Analysis

To further investigate the performance differences between the fenders, repeated impact loading–unloading simulations were conducted for the protected OWT. In engineering practice, immediate inspection, repair, or replacement of an offshore fender after a non-catastrophic collision may be restricted by high maintenance costs, limited availability of maintenance vessels, and suitable weather windows. The fender may therefore remain in service and be exposed to subsequent collisions before maintenance can be performed. Based on this engineering scenario, three successive collisions under identical conditions were simulated while retaining the structural state after each collision to evaluate the cumulative response and residual protective capacity of the unrepaired fender. To accurately reproduce the cumulative response of the tower–foundation structure under multiple ship impacts, the full-restart technique was adopted to maintain consistent boundary conditions between successive loading cycles and ensure the continuous transfer of residual stresses and deformations. After each loading–unloading cycle, the program read the d3dump file containing the final state of the preceding analysis. The stored element stresses, strains, and updated geometric configuration were then transferred to the initial state of the subsequent analysis. The same boundary conditions and loading conditions were reapplied to simulate the next collision, thereby capturing the accumulation of residual stress and deformation under repeated impacts. Figure 14 presents the stress and strain time histories of representative elements extracted from the high-stress region of the tower during three successive collisions. The results show that the rubber honeycomb sandwich fender produces higher stress peaks than the aluminum foam fender during both the initial and subsequent collisions. The corresponding strain amplitudes are also generally greater for the rubber configuration.

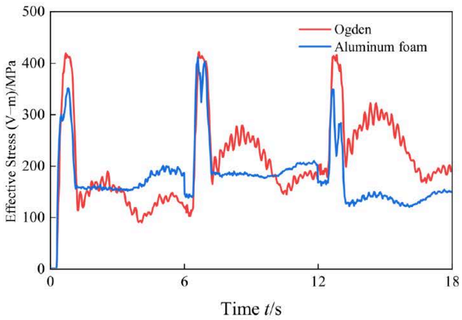

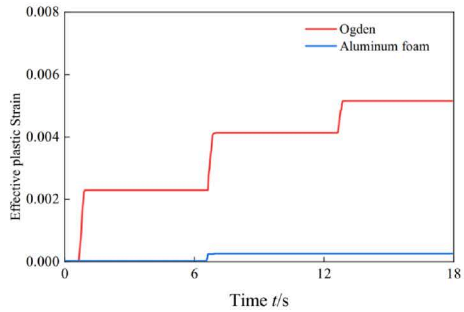

Figure 14. Stress–strain time history variation.

The von Mises stress histories exhibit pronounced fluctuations during all three collisions, with substantial differences between the two fender configurations in both peak magnitude and temporal evolution. For the rubber-core honeycomb sandwich fender, the stress in the selected tower elements rapidly reaches approximately 410 MPa during each collision and then decreases sharply. After the third collision, the residual stress remains approximately 200 MPa. The relatively low stiffness and pronounced hyperelastic recovery of the rubber core prolong load transfer and return part of the stored strain energy to the collision system, resulting in high transient stresses in the tower. By contrast, the aluminum foam core dissipates impact energy more gradually through progressive crushing and plastic collapse, producing lower stress peaks and smoother stress histories. After the third collision, the residual stress is approximately 150 MPa, which is 25% lower than that of the rubber-core configuration.

The peak stress of approximately 410 MPa exceeds the initial yield strength of Q235 steel (235 MPa), indicating that the selected tower elements enter the plastic regime. Because 235 MPa represents the onset of yielding, the stress can continue to increase after yielding owing to strain hardening. Therefore, the stress peak alone does not indicate structural failure. The corresponding effective plastic strain histories provide a more direct measure of the accumulated irreversible deformation. For the rubber-core configuration, the effective plastic strain increases stepwise during the three collisions and reaches 0.0051 after the third collision. In comparison, the aluminum foam-core configuration produces a more gradual increase, with a maximum effective plastic strain of only 0.00025. The progressive crushing and irreversible energy dissipation of the aluminum foam core therefore substantially limit the accumulation of plastic deformation in the tower.

Overall, the rubber-core fender induces higher transient stresses and greater effective plastic strain accumulation because of its relatively low stiffness and strong elastic recovery. The aluminum foam-core fender provides better tower protection during the three collisions considered, although permanent crushing progressively reduces its remaining protective capacity. These results indicate retained residual protection rather than unchanged performance after each collision. Because no separate fracture or damage criterion was applied to the tower steel, the present results characterize tower yielding and plastic strain accumulation rather than crack initiation or material failure.

6. Conclusions

Based on nonlinear dynamics theory, the explicit dynamic analysis software LS-DYNA (ANSYS LS-DYNA R13.0.0 within ANSYS 2022 R1) was employed to simulate the collision of a 5000 t ship traveling at 2 m/s with the single-column tripod foundation of an offshore wind turbine protected by honeycomb sandwich fenders with different core materials. The anti-collision characteristics of the different fenders were investigated, and the main conclusions are summarized as follows:

(1) The constitutive behavior of the core material determines the deformation mode and energy-dissipation pathway of the honeycomb fender. The rubber core primarily stores collision energy through recoverable large deformation. After unloading, most of the stored deformation energy is reconverted into the kinetic energy of the ship, resulting in a pronounced rebound effect. In contrast, the aluminum foam core dissipates energy irreversibly through cell-wall buckling, progressive crushing, and plastic collapse. The internal energy absorbed by the aluminum foam core accounts for approximately 75% of the initial kinetic energy of the ship, demonstrating a predominantly irreversible energy-dissipation pathway.

(2) The higher initial stiffness and crushing resistance of aluminum foam result in a greater peak contact force than that produced by the rubber configuration. However, its plastic crushing mechanism shortens the collision duration and reduces the maximum tower-top displacement by approximately 40%. The rubber fender decreases the instantaneous contact force, but its elastic recovery prolongs the loading process and induces more pronounced tower-top vibration. Therefore, the design of honeycomb fenders requires a comprehensive balance among peak contact force, collision duration, and irreversible energy-dissipation capacity.

(3) After three successive collisions, the residual tower stress associated with the aluminum foam configuration is approximately 25% lower than that associated with the rubber configuration, while the local strain response is also substantially suppressed. These results indicate that the progressive crushing of aluminum foam reduces the sustained transmission of collision energy to the tower and consequently mitigates the accumulation of structural responses. Overall, the aluminum foam honeycomb fender provides more favorable protection for the offshore wind turbine under the collision conditions considered in this study.

7. Limitations and Future Work

Although the present numerical analyses reveal clear differences between the protective mechanisms of rubber and aluminum foam cores, several limitations should be acknowledged. First, only one collision scenario was considered, involving a 5000 t ship traveling at 2 m/s and colliding head-on with the OWT. Consequently, the effects of ship mass, impact velocity, collision angle, and impact location were not examined. Second, the comparison was limited to two core materials with the same regular hexagonal cell geometry and fixed structural dimensions. Because the core materials have different densities, the total masses of the two fender configurations are unequal. The observed response differences therefore reflect the combined effects of material constitutive behavior and fender mass, which were not independently isolated. The influences of cell size, cell topology, face-sheet thickness, and hybrid or graded core configurations also remain unclear. Third, the hydrodynamic influence of seawater was represented using a constant added-mass coefficient of 0.05, while wave and current loads and soil–structure interaction were not explicitly modelled. In addition, the rotor–nacelle assembly was simplified using a lumped mass applied at the tower top. These assumptions may influence the global dynamic response and the transmission of collision loads through the OWT structure. Finally, the numerical model has not been directly validated against dedicated collision experiments. Therefore, the present results should be interpreted as comparative trends between the two core materials under the specified collision conditions rather than as generalized design limits.

Future work will extend the collision scenarios to include different ship masses, impact velocities, collision angles, and impact locations. Mass-equivalent fender configurations will also be examined to distinguish the influence of material behavior from that of fender mass. More comprehensive numerical models incorporating wave and current loads, direction-dependent hydrodynamic added mass, and soil–structure interaction will be developed. Material tests and scaled collision experiments will be conducted to calibrate the constitutive parameters and validate the deformation, energy-absorption, and load-transfer responses predicted by the numerical model. Furthermore, the effects of cell geometry, core arrangement, and face-sheet thickness will be investigated through multi-objective optimization to achieve a more appropriate balance among peak contact force, irreversible energy absorption, structural weight, and protection against repeated collisions.

Author Contributions: Conceptualization, K.L. and H.H.; methodology, K.L. and H.H.; software, K.L. and W.Z. (Wanyong Zhang); validation, K.L., H.H. and W.Z. (Wanyong Zhang); formal analysis, K.L. and H.H.; investigation, K.L. and W.Z. (Wanfu Zhang); resources, W.Z. (Wanfu Zhang) and C.L.; data curation, K.L. and W.Z. (Wanyong Zhang); writing—original draft preparation, K.L.; writing—review and editing, H.H., W.Z. (Wanyong Zhang), W.Z. (Wanfu Zhang) and C.L.; visualization, K.L. and W.Z. (Wanfu Zhang); supervision, H.H., W.Z. (Wanfu Zhang) and C.L.; project administration, H.H. and C.L.; funding acquisition, C.L. All authors have read and agreed to the published version of the manuscript.

Funding: This research was funded by the National Key R&D Program of China, grant number 2024YFA1012500, the National Natural Science Foundation of China, grant number 52376204, and the Program of China Scholarship Council, grant number 202508310151.

Data Availability Statement: The original contributions of this study are included in the article. Further inquiries can be directed to the corresponding author.

Acknowledgments: The authors gratefully acknowledge the computational resources provided by the Irish Centre for High-End Computing (ICHEC) at University College Cork.

Conflicts of Interest: The authors declare no conflicts of interest.

References

1. Guo, X.; Chen, X.; Chen, X.; Sherman, P.; Wen, J.; McElroy, M. Grid integration feasibility and investment planning of offshore wind power under carbon-neutral transition in China. *Nat. Commun.* **2023**, *14*, 2447. [CrossRef] [PubMed]
2. Zhang, J.; Wang, H. Development of offshore wind power and foundation technology for offshore wind turbines in China. *Ocean. Eng.* **2022**, *266*, 113256. [CrossRef]
3. Yu, Q.; Liu, K.; Chang, C.H.; Yang, Z. Realising advanced risk assessment of vessel traffic flows near offshore wind farms. *Reliab. Eng. Syst. Saf.* **2020**, *203*, 107086. [CrossRef]
4. Yue, X.; Han, Z.; Li, C.; Zhao, X. The study on structure design of fender of offshore wind turbine based on fractal feature during collision with ship. *Ocean. Eng.* **2021**, *236*, 109100. [CrossRef]
5. Moulas, D.; Shafiee, M.; Mehmanparast, A. Damage analysis of ship collisions with offshore wind turbine foundations. *Ocean. Eng.* **2017**, *143*, 149–162. [CrossRef]
6. Bela, A.; Le Sourne, H.; Buldgen, L. Ship collision analysis on offshore wind turbine monopile foundations. *Mar. Struct.* **2017**, *51*, 220–241. [CrossRef]
7. Ren, Y.; Meng, Q.; Chen, C.; Hua, X.; Zhang, Z.; Chen, Z. Dynamic behavior and damage analysis of a spar-type floating offshore wind turbine under ship collision. *Eng. Struct.* **2022**, *272*, 114815. [CrossRef]
8. Wang, J.J.; Song, Y.C.; Wang, W.; Chen, C.J. Evaluation of flexible floating anti-collision device subjected to ship impact using finite-element method. *Ocean. Eng.* **2019**, *178*, 321–330. [CrossRef]
9. Yan, S.; He, S.; Wang, D.; Wu, Y. Design and optimization of a protective device for bridge piers against debris flow impact. *Bull. Eng. Geol. Environ.* **2020**, *79*, 3321–3335. [CrossRef]
10. Liu, C.; Hao, E.; Zhang, S. Optimization and application of a crashworthy device for the monopile offshore wind turbine against ship impact. *Appl. Ocean. Res.* **2015**, *51*, 129–137. [CrossRef]
11. Han, Z.; Li, C.; Deng, Y.; Liu, J. The analysis of anti-collision performance of the fender with offshore wind turbine tripod impacted by ship and the coefficient of restitution. *Ocean. Eng.* **2019**, *194*, 106614. [CrossRef]
12. Nazir, A.; Abate, K.M.; Kumar, A.; Jeng, J.Y. A state-of-the-art review on types, design, optimization, and additive manufacturing of cellular structures. *Adv. Manuf. Technol.* **2019**, *104*, 3489–3510. [CrossRef]
13. Zhang, D.; Jiang, D.; Fei, Q.; Wu, S. Experimental and numerical investigation on indentation and energy absorption of a honeycomb sandwich panel under low-velocity impact. *Finite Elem. Anal. Des.* **2016**, *117–118*, 21–30. [CrossRef]
14. Rathod, S.; Khaire, N.; Tiwari, G. A comparative study on the ballistic performance of aramid and aluminum honeycomb sandwich structures. *Compos. Struct.* **2022**, *299*, 116048. [CrossRef]
15. Chang, B.; Wang, Z.; Bi, G. Study on the energy absorption characteristics of different composite honeycomb sandwich structures under impact energy. *Appl. Sci.* **2024**, *14*, 2832. [CrossRef]
16. Ren, N.X.; Ou, J.P. A crashworthy device against ship-OWT collision and its protection effects on the tower of offshore wind farms. *China Ocean. Eng.* **2009**, *23*, 594–602.
17. Hallquist, J.; Goudreau, G.; Benson, D. Sliding interfaces with contact-impact in large-scale Lagrangian computations. *Comput. Methods Appl. Mech. Eng.* **1985**, *51*, 107–137. [CrossRef]
18. Dai, L.; Ehlers, S.; Rausand, M.; Utne, I.B. Risk of collision between service vessels and offshore wind turbines. *Reliab. Eng. Syst. Saf.* **2013**, *109*, 18–31. [CrossRef]
19. Ye, K.; Li, C.; Yang, Y.; Zhang, W.; Xu, Z. Research on influence of ice-induced vibration on offshore wind turbines. *J. Renew. Sustain. Energy* **2019**, *11*, 033301. [CrossRef]
20. Zhao, X.; Han, Z.; Li, C.; Yue, X.; Wang, B.; Zhang, W. Research on protection performance of via hole fender for offshore wind turbine. *Proc. CSEE* **2021**, *41*, 5624–5633.
21. Han, Z.; Zhao, X.; Li, C.; Ding, Q. Effects on the Various Aluminum Foam Fenders of a Tripod Offshore Wind Turbine Collision Due to a Ship. *Mar. Technol. Soc. J.* **2020**, *54*, 79–96. [CrossRef]

22. Lim, H.K.; Lee, J.S. On the structural behavior of ship's shell structures due to impact loading. *Int. J. Nav. Archit. Ocean. Eng.* **2018**, *10*, 103–118. [CrossRef]
23. Gladman, B. *LS-DYNA Keyword User's Manual: Volume I, Version 971*; Livermore Software Technology Corporation: Livermore, CA, USA, 2007.
24. Ogden, R. *Non-Linear Elastic Deformations*; Courier Corporation: Chelmsford, MA, USA, 1997.
25. García-Moreno, F. Commercial applications of metal foams: Their properties and production. *Materials* **2016**, *9*, 85. [CrossRef] [PubMed]
26. Deshpande, V.S.; Fleck, N.A. High strain rate compressive behaviour of aluminum alloy foams. *Int. J. Impact Eng.* **2000**, *24*, 277–298. [CrossRef]
27. *DNV-RP-C204*; Design Against Accidental Loads. Det Norske Veritas: Hovik, Norway, 2010.
28. Hao, E.; Liu, C. Evaluation and comparison of anti-impact performance to offshore wind turbine foundations: Monopile, tripod, and jacket. *Ocean. Eng.* **2017**, *130*, 218–227. [CrossRef]
29. *DNV-OS-J101*; Design of Offshore Wind Turbine Structures. Det Norske Veritas: Hovik, Norway, 2011; pp. 26–34.
30. Nokob, M.H.; Yeung, R.W. Added mass of thin flat plates of arbitrary shapes with possible openings. *Appl. Ocean. Res.* **2018**, *79*, 149–159. [CrossRef]
31. Zhang, S.; Villavicencio, R.; Zhu, L.; Pedersen, P.T. Ship collision damage assessment and validation with experiments and numerical simulations. *Mar. Struct.* **2019**, *63*, 239–256. [CrossRef]
32. Zhang, W.; Li, R.; Yang, Q.; Fu, Y.; Kong, X. Impact resistance of a fiber metal laminate skin bio-inspired composite sandwich panel with a rubber and foam dual core. *Materials* **2023**, *16*, 453. [CrossRef] [PubMed]